Volume 18
Number 6
21 March 2025
Pages 2637–3048

Energy & Environmental Science

rsc.li/ees

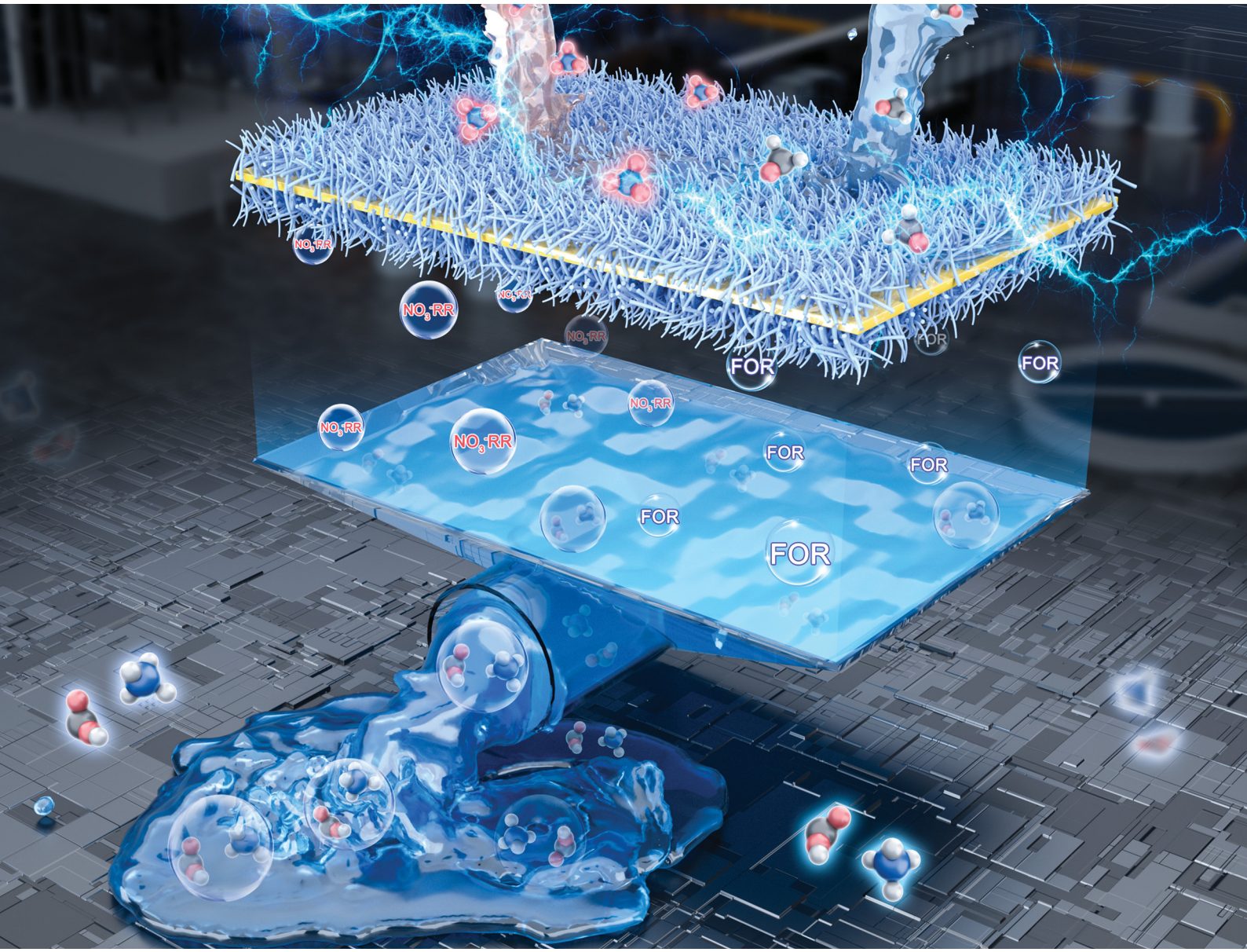

ISSN 1754-5706

ROYAL SOCIETY OF CHEMISTRY

PAPER

Lili Han *et al.*

Unlocking high-current-density nitrate reduction and formaldehyde oxidation synergy for scalable ammonia production and fixation

Energy & Environmental Science

ROYAL SOCIETY OF CHEMISTRY

PAPER

View Article Online
View Journal | View Issue

Cite this: *Energy Environ. Sci.*, 2025, **18**, 2804

Unlocking high-current-density nitrate reduction and formaldehyde oxidation synergy for scalable ammonia production and fixation†

Linjie Zhang, ‡[a] Yimeng Cai,‡[a] Yanghua Li,[a] Chen Sun,[a] Yi Xiao,[a] Yibing Yang,[a] Dechao Chen,[a] Dongdong Xiao,[b] Chi-Feng Lee, [c] Yunjian Wang,[a] Shiqiang Feng,[a] Hsiao-Tsu Wang, [c] Yu-Cheng Shao,[d] Ting-Shan Chan,[d] Hirofumi Ishii,[d] Nozomu Hiraoka,[d] Xiuyun Wang,[e] Jun Luo [f] and Lili Han *[a]

Nitrate electroreduction to ammonia holds great promise in sustainable green ammonia synthesis, yet faces a dearth of competent electrocatalysts adapted to varying nitrate concentration, and inadequate ammonia fixation. Herein, we present a high-performance Ag single-atom-decorated Cu_2O nanowire catalyst ($Ag_1@Cu_2O$) that exhibits concentration-universal high-rate nitrate reduction, achieving >90% to near-unity ammonia faradaic efficiency (FE) across nitrate concentrations from 0.01 to 0.5 M. Notably, at 0.5 M nitrate concentration, it attains a two-ampere-level current density (2.3 A cm^{-2}) at −1 V *vs.* RHE, resulting in a leading ammonia yield rate of 184.4 mg_{NH_3} h^{-1} cm^{-2}. *In situ* studies combined with theoretical calculations elucidate an Ag–Cu inter-site synergistic catalytic mechanism, in which single-atom Ag serves as an accelerator for active hydrogen generation and stabilization on Cu sites to boost the hydrogenation kinetics of N-containing intermediates, thus smoothing the energy barriers for ammonia production *via* the favorable *NHO pathway. Additionally, $Ag_1@Cu_2O$ demonstrates near-unity formate FE for formaldehyde oxidation, reaching a 300 mA cm^{-2} current density at a mere 0.31 V *vs.* RHE. Motivated by this exceptional bifunctionality, we demonstrate an innovative tandem electrochemical–chemical strategy for upgrading ammonia into high-value ammonium formate by coupled electrolysis of nitrate reduction and formaldehyde oxidation, followed by straightforward chemical combination and isolation. In practice, membrane electrode assembly (MEA) electrolysis at 1.6 V for 100 h successfully outputs 10.7 g of high-purity ammonium formate. Furthermore, the commonality of this strategy is validated by application to various nitrate/aldehyde pairs. This work blazes a new trail for scalable, cost- and energy-efficient green ammonia production and fixation from nitrate reduction.

Received 25th September 2024,
Accepted 20th January 2025

DOI: 10.1039/d4ee04382k

rsc.li/ees

Broader context

Ammonia electrosynthesis from nitrate reduction presents a promising alternative to the energy-intensive and stringent Haber–Bosch process. However, it necessitates high-performance electrocatalysts, and the efficient extraction and storage of ammonia from the electrolyte remain critical challenges. In this study, we developed an Ag single-atom-decorated Cu_2O nanowire catalyst capable of ammonia production at a current density exceeding 2 A cm^{-2}, and showcased a tandem electrochemical–chemical route to upgrade ammonia into high-purity ammonium formate on a 10 g-scale by coupling cathodic nitrate reduction and anodic formaldehyde oxidation in a membrane assembly electrolyzer. Moreover, we elucidated the Ag–Cu inter-site synergistic catalytic mechanism for the high-rate nitrate reduction, and verified the broad adaptability of the route for upgrading ammonia into various other ammonium salts.

[a] *State Key Laboratory of Structural Chemistry, Fujian Institute of Research on the Structure of Matter, Chinese Academy of Sciences, Fuzhou 350002, China. E-mail: llhan@fjirsm.ac.cn*
[b] *Beijing National Laboratory for Condensed Matter Physics, Institute of Physics, Chinese Academy of Sciences, Beijing 100190, China*
[c] *Department of Physics, Tamkang University, New Taipei City 251301, Taiwan*
[d] *National Synchrotron Radiation Research Center, Hsinchu 300092, Taiwan*
[e] *National Engineering Research Center of Chemical Fertilizer Catalyst, Fuzhou University, Fuzhou 350002, China*
[f] *ShenSi Lab, Shenzhen Institute for Advanced Study, University of Electronic Science and Technology of China, Longhua District, Shenzhen 518110, China*

† Electronic supplementary information (ESI) available. See DOI: https://doi.org/10.1039/d4ee04382k

‡ These authors contributed equally to this work.

Introduction

Ammonia (NH_3) stands as a cornerstone of the N-fertilizer industry and a promising energy vector, yet the industrial Haber–Bosch process used for its synthesis is characterized by high energy consumption and carbon emissions.[1–3] A promising alternative is the electrosynthesis of green NH_3 *via* the nitrate (NO_3^-) reduction reaction (NO_3^-RR) using renewable electricity under ambient conditions.[4–6] NO_3^-, often found in industrial and domestic sewage, can cause severe nitrogen pollution to the environment if not disposed of properly.[7,8] Converting this "NO_3^- trash" into "NH_3 treasure" offers an economic and sustainable solution, also aiding in maintaining the nitrogen cycle. However, the efficiency of the electrochemical NO_3^-RR is plagued by keen competition with the hydrogen evolution reaction (HER) and varying NO_3^- levels in diverse sewage sources.[9,10] Hence, developing highly active and concentration-universal electrocatalysts capable of high-rate NO_3^--to-NH_3 conversion is crucial.

Besides the rational architecture of high-performance electrocatalysts, the efficient fixation of the produced NH_3 is equally important but has been largely overlooked.[11,12] As with hydrogen energy storage, the direct storage of liquid NH_3 is both inconvenient and energy intensive. A more viable approach is to transform liquid NH_3 into solid ammonium salts for its chemical storage and value-added conversion. Currently, very limited NH_3 fixation routes for electrochemical NO_3^-RR have been developed, generally including (1) Ar- or air-assisted stripping of gaseous NH_3 from the electrolyte post-electrolysis, followed by acid or CO_2 trapping and subsequent transformation into solid NH_4Cl, $(NH_4)_2SO_4$ or NH_4HCO_3 through rotary evaporation;[2,13–15] (2) direct treatment of the electrolyte post-electrolysis with external chemicals to convert NH_3 into $MgNH_4PO_4$ fertilizer.[16,17] Despite these advances, existing routes primarily produce basic ammonium fertilizers, which lack sufficient value-added benefits, and the involved purification and isolation processes are cumbersome and inefficient, necessitating considerable external feedstock input and increasing production costs. Furthermore, their low current densities of NO_3^-RR hamper scalable NH_3 production and fixation. More importantly, the paired anodic oxygen evolution reaction (OER) is both thermodynamically unfavorable and kinetically sluggish, which not only pulls down the energy efficiency for NH_3 electrosynthesis but also yields relatively valueless O_2 byproduct.[18,19] These challenges highlight the urgent need for new strategies to address the inefficiencies in NH_3 production and fixation from routine NO_3^-RR.

Herein, we present an innovative tandem electrochemical–chemical synthetic strategy for scalable, energy-efficient and cost-effective upgrading of NH_3 from NO_3^-RR into high-value pure ammonium formate ($HCOONH_4$) solid. This approach aimfully pairs the formaldehyde (HCHO) oxidation reaction (FOR) to NO_3^-RR in a coupled electrolysis, followed by a set of straightforward chemical processes to realize NH_3 fixation (Fig. 1(a)). HCHO, the main downstream product of methanol and a basic chemical raw material in industry, is also a notorious pollutant prevalent in various industrial sewage effluents and off-gases. However, it is found that the thermodynamic equilibrium potential of FOR ($2HCHO + 4OH^- - 2e^- \rightarrow 2HCOO^- + H_2 + 2H_2O$, $E^\circ = -0.22$ V *vs.* RHE) is significantly lower than that of OER (1.23 V_{RHE}).[20] Consequently, the pairing with anodic FOR not only facilitates the concurrent elimination of HCHO contaminant but also significantly enhances the energy efficiency for NH_3 production. Additionally, FOR produces valuable formate and H_2 products in the anodic chamber, motivating us to conceive of the further combination of anodic formate with cathodic NH_3, along with subsequent

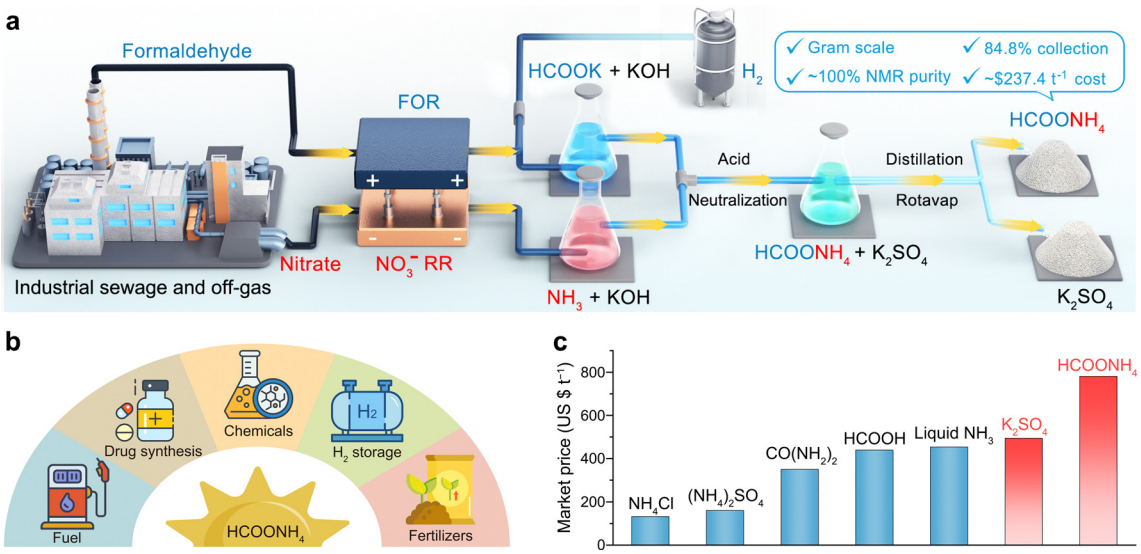

Fig. 1 Paired nitrate reduction and formaldehyde oxidation for scalable green NH_3 production and fixation into high-value ammonium formate ($HCOONH_4$). (a) Workflow overview of the tandem electrochemical–chemical upgrading of nitrate and formaldehyde into $HCOONH_4$ solid at a 10 g scale. (b) Examples of diverse industrial benefits of $HCOONH_4$. (c) Comparison of market values of $HCOONH_4$ with other inorganic ammonium acid salts and related chemicals in 2024.

chemical steps, including acid neutralization, distillation and rotary evaporation, to give the desired $HCOONH_4$ product. Notably, $HCOONH_4$ is not just an N-fertilizer and NH_3 carrier, it also finds extensive applications in fuel cells, hydrogen storage, chemical synthesis (*e.g.*, formamide synthesis upon heating), pharmaceuticals, *etc* (Fig. 1(b)).[21–23] In comparison to those previously obtained inorganic ammonium salts from the routine NO_3^-RR process, $HCOONH_4$ commands a considerably higher market value, reaching approximately \$800 per ton (Fig. 1(c) and Table S1, ESI†). Moreover, the isolation of $HCOONH_4$ allows for the simultaneous recovery of a pure K_2SO_4 solid byproduct, thus further enhancing the economic efficiency of this route for NH_3 fixation.

To implement this proof-of-concept, we have synthesized Ag single-atom-decorated Cu_2O nanowires ($Ag_1@Cu_2O$ NWs) densely grown on Cu foam, which serve as a high-performance bifunctional electrocatalyst for both NO_3^-RR and FOR. This catalyst design is motivated primarily by the demonstrated high activity of Cu alloys for both reactions, combined with the benefits of atomic-level electronic structure modulation by single-atom incorporation.[24–26] Remarkably, $Ag_1@Cu_2O$ NWs showcase concentration-universal high NO_3^-RR electrocatalytic activity, demonstrating a fast reaction rate and near-unity NH_3 faradaic efficiency (FE) at low overpotential in low NO_3^--level electrolytes, and a two-ampere-level current density of 2.3 A cm^{-2} coupled with an ultrahigh NH_3 yield rate of 184.4 mg_{NH_3} h^{-1} cm^{-2} in high NO_3^--level electrolyte (0.5 M). The results of a series of *in situ* experiments and density functional theory (DFT) calculations reveal the pivotal role of single-atom Ag in inhibiting HER while facilitating the hydrogenation of N-containing intermediates adsorbed on Cu sites, leading to the high rate of NH_3 production. Meanwhile, in the FOR electrocatalysis, it secures near-100% FE for both formate and H_2 production with a large current density of 300 mA cm^{-2} at 0.31 V (*vs.* RHE, hereafter the same potential scale is used without iR-compensation). Leveraging the high rate, high FE and high current density afforded by $Ag_1@Cu_2O$ NWs, membrane electrode assembly (MEA)-based paired NO_3^-RR/FOR electrolysis at 1.6 V_{cell} for 100 h successfully achieves the gram-scale synthesis of high-purity $HCOONH_4$ solid (10.7 g), with a high collection efficiency of 84.8% and a low production cost of \$237.4 t^{-1}, based on a techno-economic analysis. Moreover, this route can be further extended to pairs of NO_3^-RR with anodic oxidation reactions of two other representative heterocyclic aldehydes of 4-pyridinecarboxaldehyde (4-PCA) and 5-hydroxymethylfurfural (HMF).

Results and discussion

Synthesis and structural analyses of $Ag_1@Cu_2O$ NWs

The $Ag_1@Cu_2O$ NWs were synthesized by densely growing $Cu(OH)_2$ nanowires on a low-cost Cu foam substrate, followed by immersing it into an $AgNO_3$ solution and a subsequent low-temperature reduction process using H_2/Ar at 200 °C (for experimental details, see Materials and methods and Fig. S1 and S2, ESI†). Scanning electron microscopy (SEM) analysis confirmed the dense and uniform nanowire morphology of the $Ag_1@Cu_2O$ NWs, with an approximate length of 4.5 μm and a width of 172 nm (Fig. 2(a)). The interwoven nanowires construct a highly conductive network, facilitating the rapid charge transfer essential for catalytic activity. Compared to smooth pristine Cu_2O NWs, the integration of Ag single-atoms significantly increases the surface roughness of $Ag_1@Cu_2O$ NWs (Fig. S3, ESI†), thereby enhancing the exposure of active sites for catalysis. To scrutinize the surface details of $Ag_1@Cu_2O$ NWs, a three-dimensional (3D) electron tomographic reconstruction was performed using a series of two-dimensional (2D) transmission electron microscopy (TEM) images of a single nanowire (Movie S1, ESI†). The volume-rendering images reveal a distinct pentagon-like star-shaped cross-section with extensive porosity in $Ag_1@Cu_2O$ NWs (Fig. 2(b)). The internal pore volume within a single nanowire exceeds 35%, conferring upon $Ag_1@Cu_2O$ NWs an intricate porous configuration that offers abundant active sites and efficient mass transport channels, thereby favoring enhanced catalytic reaction kinetics (Fig. S4, ESI†).[27]

X-ray diffraction (XRD) analysis revealed a compositional transition from $Cu(OH)_2$ NWs to Cu_2O NWs following H_2/Ar reduction (Fig. S5, ESI†). Furthermore, the absence of metallic Ag or its corresponding oxide in $Ag_1@Cu_2O$ NWs was confirmed, indicating the presence of Ag single-atoms. This observation was further substantiated by energy-dispersive spectroscopy (EDS) mapping, which shows an even distribution of Ag atoms across the entire surface of $Ag_1@Cu_2O$ NWs (Fig. 2(c)). The Ag mass loading in $Ag_1@Cu_2O$ NWs was determined at 0.25 wt% using inductively coupled plasma optical emission spectroscopy (ICP-OES) (Table S2, ESI†). Such notably low Ag content greatly contributes to the cost-effective synthesis of $Ag_1@Cu_2O$ NWs (Table S3, ESI†). The high-angle annular dark-field scanning TEM (HAADF-STEM) imaging revealed that the topography of $Ag_1@Cu_2O$ NWs closely resembles that reconstructed by 3D electron tomography (Fig. 2(d) and Fig. S6, ESI†). Furthermore, lattice analysis of $Ag_1@Cu_2O$ NWs using the aberration-corrected-HAADF-STEM (AC-HAADF-STEM) image and the corresponding fast Fourier transform (FFT) unveiled lattice spacings of 0.215 and 0.246 nm, attributed to the (200) and (111) planes of an fcc-type Cu_2O (Fig. 2(e) and (f)), in line with the XRD results. Additionally, a multitude of distinct bright spots was recognized on the surface of $Ag_1@Cu_2O$ NWs, indicating an isolated dispersion of Ag single-atoms rather than clusters, a result of substituting Ag atoms for Cu atoms within the Cu_2O lattice.[13] This observation was further supported by the line intensity profile in the region of interest, revealing a significant variation in *Z*-lining between atoms, correlating directly with the disparity in atomic numbers between Ag and Cu elements (Fig. 2(g)).[28]

The fine local electronic and coordination structure of $Ag_1@Cu_2O$ NWs was further probed by synchrotron X-ray absorption near-edge structure (XANES) spectra at both the Cu K-edge and Ag K-edge. The Cu K-edge profiles of $Ag_1@Cu_2O$ NWs, Cu_2O NWs and reference Cu_2O exhibit close proximity, manifesting a similar rising-edge shoulder at 8981 eV, indicating comparable Cu valences with the same tetrahedral coordination

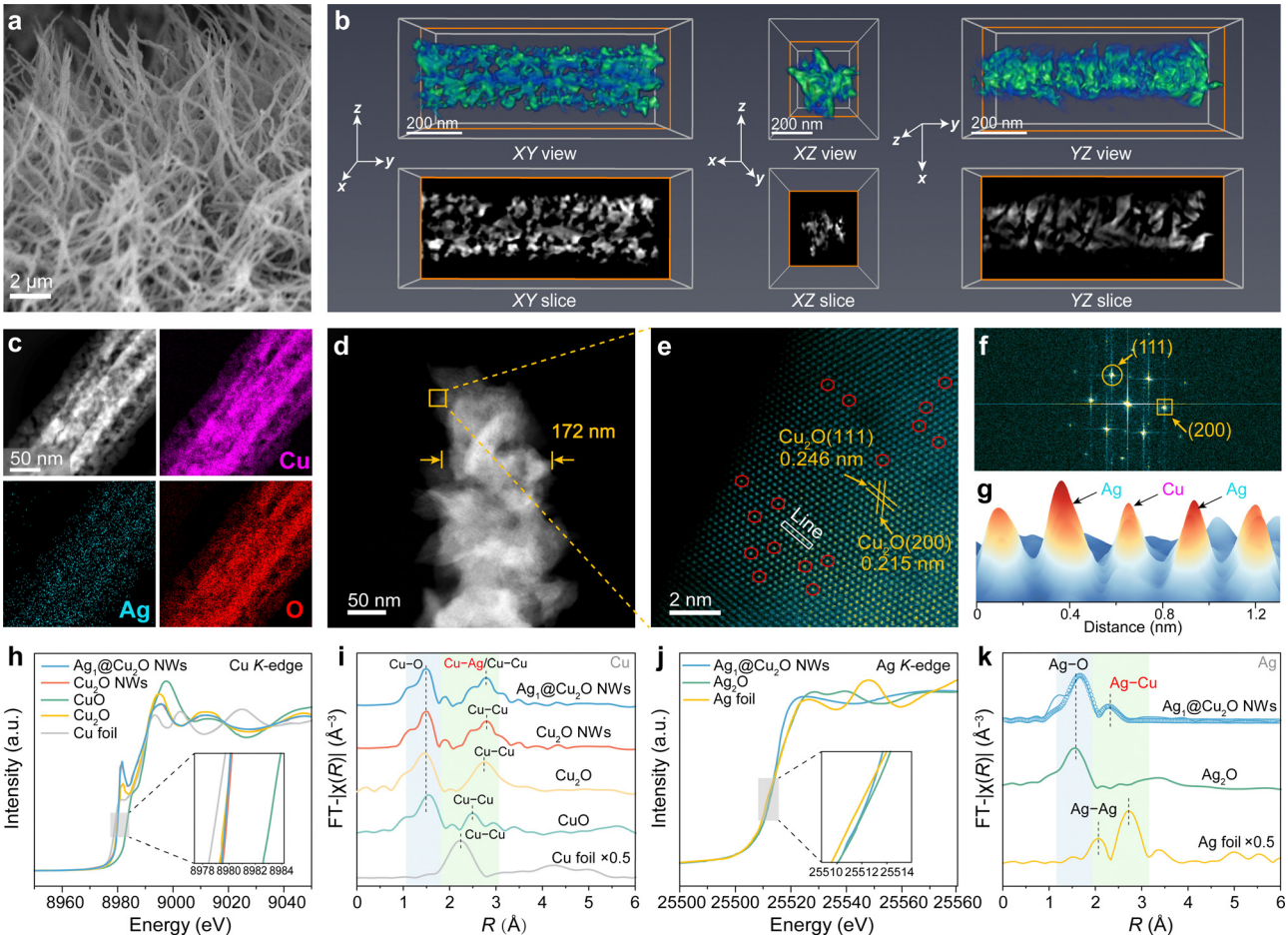

Fig. 2 Structural analyzes of $Ag_1@Cu_2O$ NWs. (a) SEM image. (b) 3D electron tomographic reconstruction. (c) EDS mappings. (d) HAADF-STEM image. (e) AC-HAADF-STEM image. (f) Corresponding FFT pattern and (g) intensity profile along the line indicated in panel (e). (h) XANES and (i) FT-EXAFS spectra at the Cu K-edge. (j) XANES and (k) FT-EXAFS spectra at the Ag K-edge; the circle in panel (k) represents the best-fitting data.

geometry (Fig. 2(h)).[29] In contrast, the shoulder for reference CuO appears at 8986 eV, reflecting a distinct square planar coordination geometry. Compared to Cu_2O NWs, the slight low-energy shift of the Cu K-edge of $Ag_1@Cu_2O$ NWs suggests increased electron density donated from Ag single-atoms to the Cu_2O support due to their strong electronic interaction, which was further confirmed by XPS analysis (Fig. S7–S9, ESI†).[30] In the *R*-space of the Fourier-transformed (FT) k^3-weighted extended X-ray absorption fine structure (EXAFS) spectra at the Cu K-edge (Fig. 2(i)), $Ag_1@Cu_2O$ NWs display two pronounced peaks at approximately 1.50 and 2.78 Å, corresponding to Cu–O and Cu–Ag/Cu–Cu bonding in the first coordination shell, respectively. Correspondingly, the Ag K-edge XANES spectrum of $Ag_1@Cu_2O$ NWs emerges between those of Ag foil and Ag_2O (Fig. 2(j)). Additionally, the Ag K-edge FT-EXAFS spectrum of $Ag_1@Cu_2O$ NWs exhibits a major peak around 1.5 Å and a minor peak at approximately 2.3 Å, which are assigned to Ag–O and Ag–Cu scattering, respectively (Fig. 2(k)). This result was further confirmed by the wavelet transform EXAFS (WT-EXAFS) spectrum of $Ag_1@Cu_2O$ NWs (Fig. S10, ESI†). Corresponding EXAFS fitting analysis revealed coordination numbers of 1.69 for Ag–O and 1 for Ag–Cu shells (Table S4, ESI†). Importantly, the absence of a peak for Ag–Ag bonding indicates that Ag atoms are integrated into the Cu_2O lattice as isolated single-atoms *via* ion exchange (Fig. S11, ESI†), effectively precluding the formation of clusters or nanoparticles.

Electrocatalytic NO_3^-RR performance

The electrocatalytic NO_3^-RR performance of $Ag_1@Cu_2O$ NWs, and the control samples of Cu_2O NWs and Cu foam were initially assessed in an electrolyte composed of 1 M KOH with 250 mM KNO_3 using a three-electrode testing system. The linear sweep voltammetry (LSV) results depicted in Fig. 3(a) revealed a significant disparity in current densities among the samples. Notably, $Ag_1@Cu_2O$ NWs exhibited the highest current density across all potentials, reaching an ampere-level 1.74 A cm^{-2} at −1 V, followed by the inferior Cu_2O NWs, while Cu foam lagged far behind. Subsequently, variations in the concentrations of NO_3^- reactant, NO_2^- intermediate, and NH_3 product during the NO_3^-RR at multiple potentials in chronoamperometry tests were analyzed by UV-vis absorption spectroscopy (Fig. S12–S14, ESI†). Accordingly, the calculated NH_3 faradaic efficiency (FE) on $Ag_1@Cu_2O$ NWs showed a progressive increase from −0.1 to −0.6 V, followed by a stable

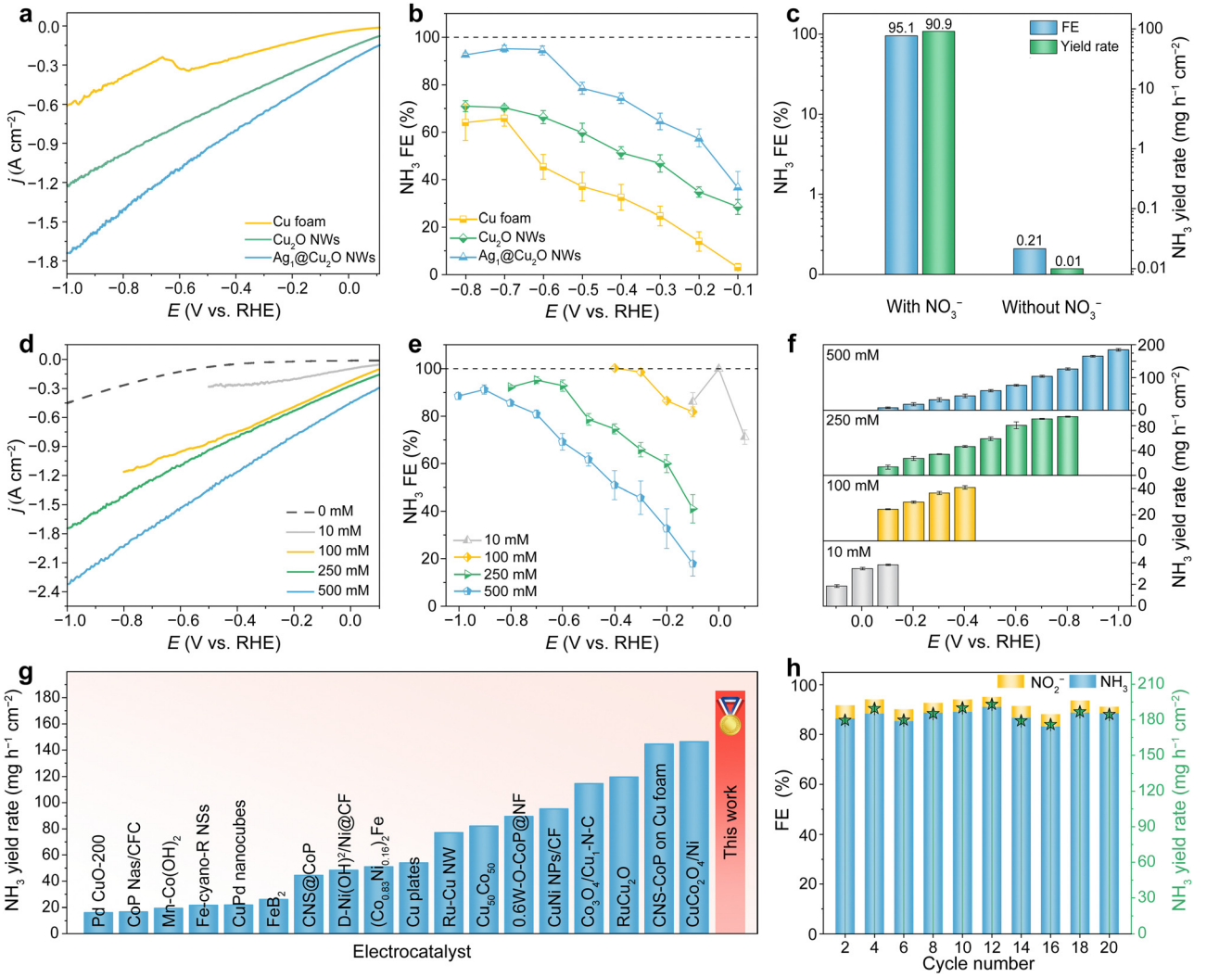

Fig. 3 Electrocatalytic NO_3^-RR performance. (a) LSVs on Ag_1@Cu_2O NWs, Cu_2O NWs, and Cu foam in 1 M KOH with 250 mM NO_3^-. (b) NH_3 FEs on Ag_1@Cu_2O NWs, Cu_2O NWs, and Cu foam in 1 M KOH with 250 mM NO_3^-. (c) NH_3 FEs and yield rates on Ag_1@Cu_2O NWs in 1 M KOH with and without 250 mM NO_3^- at −0.7 V. (d) LSVs, (e) NH_3 FEs and (f) NH_3 yield rates on Ag_1@Cu_2O NWs in 1 M KOH with varying NO_3^- concentration. (g) Comparison of NH_3 yield rate on Ag_1@Cu_2O NWs with those of reported electrocatalysts. (h) NH_3 FEs and yield rates during 20 periods of 1 h continuous stability measurement for Ag_1@Cu_2O NWs at −1 V in 1 M KOH with 500 mM NO_3^-. Error bars represent the standard deviation of at least three independent measurements, with the central value being their average.

plateau up to −0.8 V, with a maximum of 95.1% at −0.7 V (Fig. 3(b)). Thereby, the NH_3 yield rate on Ag_1@Cu_2O NWs achieved a maximum value of 90.88 mg h^{-1} cm^{-2} at −0.8 V, significantly surpassing those of Cu_2O NWs (55.12 mg h^{-1} cm^{-2}) and Cu foam (26.69 mg h^{-1} cm^{-2}) by 1.9 and 4.6 folds, respectively (Fig. S15, ESI†). Noticeably, Cu foam predominantly produced intermediate NO_2^- with FEs ranging from 50% to 90% between −0.1 and −0.6 V, and only achieves a mediocre NH_3 FE around 60% at more negative potentials (Fig. S16, ESI†). This is likely to be due to the insufficient *H adsorption capacity of Cu alone, which retards the hydrogenation of intermediates, such as $*NO_3$, $*NO_2$, and *NHO.[31,32] While Cu_2O NWs showed much improved NH_3 FEs compared to Cu foam, they remained below 70%. Comparatively, the remarkably enhanced NO_3^-RR activity of Ag_1@Cu_2O NWs can be primarily attributed to the integration of Ag single-atoms within the Cu_2O lattice, which facilitates rapid hydrogenation of the NO_2^- intermediate for efficient NH_3 conversion. This boost in reaction kinetics was corroborated using electrochemical impedance spectroscopy (EIS), which provided evidence for the lowest charge transfer resistance for Ag_1@Cu_2O NWs among the samples (Fig. S17, ESI†). Notably, the superiority of Ag_1@Cu_2O NWs was confirmed by a series of catalyst screenings, including control over the growth density of Cu_2O NWs, adjusting Ag loadings, incorporating Ag into other metal foams, incorporating Co nanoparticles onto Cu_2O NWs, and comparing with planar Ag (Fig. S18–S22, ESI†).

In addition, the authenticity of NH_3 originating from the NO_3^-RR process was confirmed by a comparative experiment in 1 M KOH solution without NO_3^- at −0.7 V, which showed negligible NH_3 production (Fig. 3(c)). This evidence was further reinforced by an $^{15}NO_3^-$ isotopic labeling experiment, coupled with both qualitative and quantitative NH_3 analysis using

^{1}H nuclear magnetic resonance (NMR) spectroscopy (Fig. S23–S26, ESI†).

In practical industrial sewage, NO_3^- levels may vary by source. Hence, the adaptability of $Ag_1@Cu_2O$ NWs to different NO_3^- concentrations (10, 100 and 500 mM) was further examined. As illustrated in Fig. 3(d), LSV results indicate that the current density increases with rising NO_3^- concentration. Notably, at 500 mM, the current density at −1 V reaches an ultrahigh two-ampere-level of 2.3 A cm^{-2}, a magnitude rarely observed in the NO_3^-RR domain. Further quantitative analysis revealed prevailing NH_3 production post −0.3 V, reaching a peak NH_3 FE of 91.2% at −0.9 V (Fig. 3(e) and Fig. S27, S28, ESI†). As a result of the high current density and FE, $Ag_1@Cu_2O$ NWs afford an excellent NH_3 yield rate of 184.4 mg h^{-1} cm^{-2} at −1 V, far higher than the vast majority of previously reported values (Fig. 3(f), (g) and Table S5, ESI†). Moreover, at lower 10 mM and 100 mM NO_3^- concentrations, both near-unity (100 ± 1%) NH_3 FEs could be obtained on $Ag_1@Cu_2O$ NWs at low potentials of 0 V and −0.4 V (Fig. 3(e)), respectively, with corresponding NH_3 yield rates of 3.45 and 40.75 mg h^{-1} cm^{-2} (Fig. 3(f)). At a more negative potential of −0.1 V with the 10 mM NO_3^- concentration, the NH_3 FE abruptly decreases to 86.1% (Fig. 3(e)), indicating the occurrence of HER due to fast depletion of NO_3^- that cannot sustain long-term electrolysis. Consequently, nearly 100% NO_3^--to-NH_3 conversion can be achieved within 1 h (Fig. S29, ESI†), reducing NO_3^- levels to below 50 ppm in these two electrolytes, thereby meeting the World Health Organization's prescribed threshold for drinking water.[33] Notably, compared to the low NO_3^- concentrations, the slightly declined NH_3 FE at the 500 mM high NO_3^- concentration might be attributed to the crowded NO_3^- adsorption on active sites, which impedes subsequent hydrogenation and desorption of intermediates.[34] Nevertheless, the above results strongly demonstrate the exceptional performance of $Ag_1@Cu_2O$ NWs for concentration-universal high-rate NO_3^--to-NH_3 conversion.

Furthermore, the stability of $Ag_1@Cu_2O$ NWs was rigorously examined in 1 M KOH and 500 mM NO_3^- at −1 V. As shown in Fig. 3(h), during 20 repeated cycles with each lasting for 1 h, both the NH_3 FEs and yield rates exhibited only slight fluctuations, indicating the high reusability and durability of $Ag_1@Cu_2O$ NWs. TEM and EDS mapping confirmed that the spent $Ag_1@Cu_2O$ NWs retained their intact nanowire structure with atomically dispersed Ag atoms (Fig. S30, ESI†). Electron energy loss spectroscopy (EELS) mappings coupled with HRTEM images revealed that the nanowire surfaces were partially reduced to Cu^0, leading to *in situ* restructuring into a tandem Cu^0/Cu^{1+} heterostructure (Fig. S31, ESI†). Previous studies have shown that electron transfer at the Cu/Cu_2O interface favors the formation of the key *NHO intermediate and meanwhile suppresses *H dimerization to increase the proton supply during the NO_3^-RR process.[35,36] Thus, it is hypothesized that the superior NO_3^--to-NH_3 conversion performance of $Ag_1@Cu_2O$ NWs across diverse concentrations might be attributed to the synergistic contribution of the Ag single-atoms and the unique Cu/Cu_2O tandem structure, together with the high abundance of active sites and electrical conductivity offered by the advantageous elongated nanowire structure seamlessly planted onto the Cu foam.

Mechanistic study of NO_3^-RR

To elucidate the origin of the activity underlying such outstanding performance of $Ag_1@Cu_2O$ NWs, a series of *in situ* experiments were conducted to probe the dynamic valence and structural evolution of the Cu and Ag sites, as well as the N-containing reaction intermediates during NO_3^-RR. Initially, *in situ* high-energy resolution fluorescence detected (HERFD) synchrotron XANES spectra were analyzed (Fig. S32, ESI†). As shown in Fig. 4(a), as the potential progressively decreases from open circuit potential (OCP) to −0.2 V and −0.4 V, the Cu K-edge exhibits a gradual shift to lower energies, indicating a reduction in Cu valence state, with some Cu^{1+} being reduced to Cu^0. Additionally, we conducted linear fitting of normalized XANES spectra at different potentials using Cu foil and Cu_2O as references to determine the potential-dependent apparent oxidation states of $Ag_1@Cu_2O$ catalysts (Fig. S33, ESI†). The fitting results indicate that as the potential shifts negatively, $Ag_1@Cu_2O$ NWs exhibit a gradual decrease in oxidation valence, suggesting that some Cu_2O is reduced to Cu, thereby forming a tandem Cu/Cu_2O heterostructure. This finding echoes the above TEM/EELS mapping analysis. Conversely, the Ag K-edge continuously shifts to higher energies from OCP to −0.2 V and then −0.4 V (Fig. 4(b)), indicating the gradually increased oxidation state of Ag single-atoms with decreasing potential. This indicates that there exists continuous electron transfer from Ag single-atoms to neighboring Cu atoms as the potential decreases, suggesting that both Cu atoms and Ag single-atoms might serve as active sites during the NO_3^-RR processes. Subsequent quasi-*in situ* electron paramagnetic resonance (EPR) analysis revealed that $Ag_1@Cu_2O$ NWs exhibited a pronounced *H signal in the absence of NO_3^-, which was then markedly attenuated upon the addition of NO_3^- (Fig. 4(c)). This indicates that $Ag_1@Cu_2O$ NWs could speed the formation of active *H, which are then rapidly consumed during the hydrogenation steps in the NO_3^-RR process. In contrast, the indigenous active *H formation on Cu_2O NWs hampers further hydrogenation, thereby explaining its high NO_2^- FE.[14,37] Combining the results from *ex situ*/*in situ* XANES and quasi-*in situ* EPR analyses, it can be reasonably inferred that Ag single-atoms act as an accelerator to facilitate H_2O dissociation and subsequent active *H generation and stabilization on neighboring Cu^0 atoms, due to their significant electronic interactions and a theoretical consideration of the relatively greater *H binding strength of metallic Cu compared to Ag. Whereas cationic Cu^{1+} atoms function as the primary active sites for the adsorption of anionic NO_3^- and the subsequently evolved N-containing intermediates. During NO_3^-RR, the active *H formed on Cu^0 sites flow continuously across the Cu/Cu_2O heterointerface to the $*NO_3^-$ adsorbed on Cu^{1+} sites for their stepwise hydrogenation. This cooperative inter-site synergy facilitates the further conversion of $*NO_2^-$ intermediates that is stagnant on Cu_2O alone, thereby improving the reactivity and NH_3 FE for NO_3^-RR.

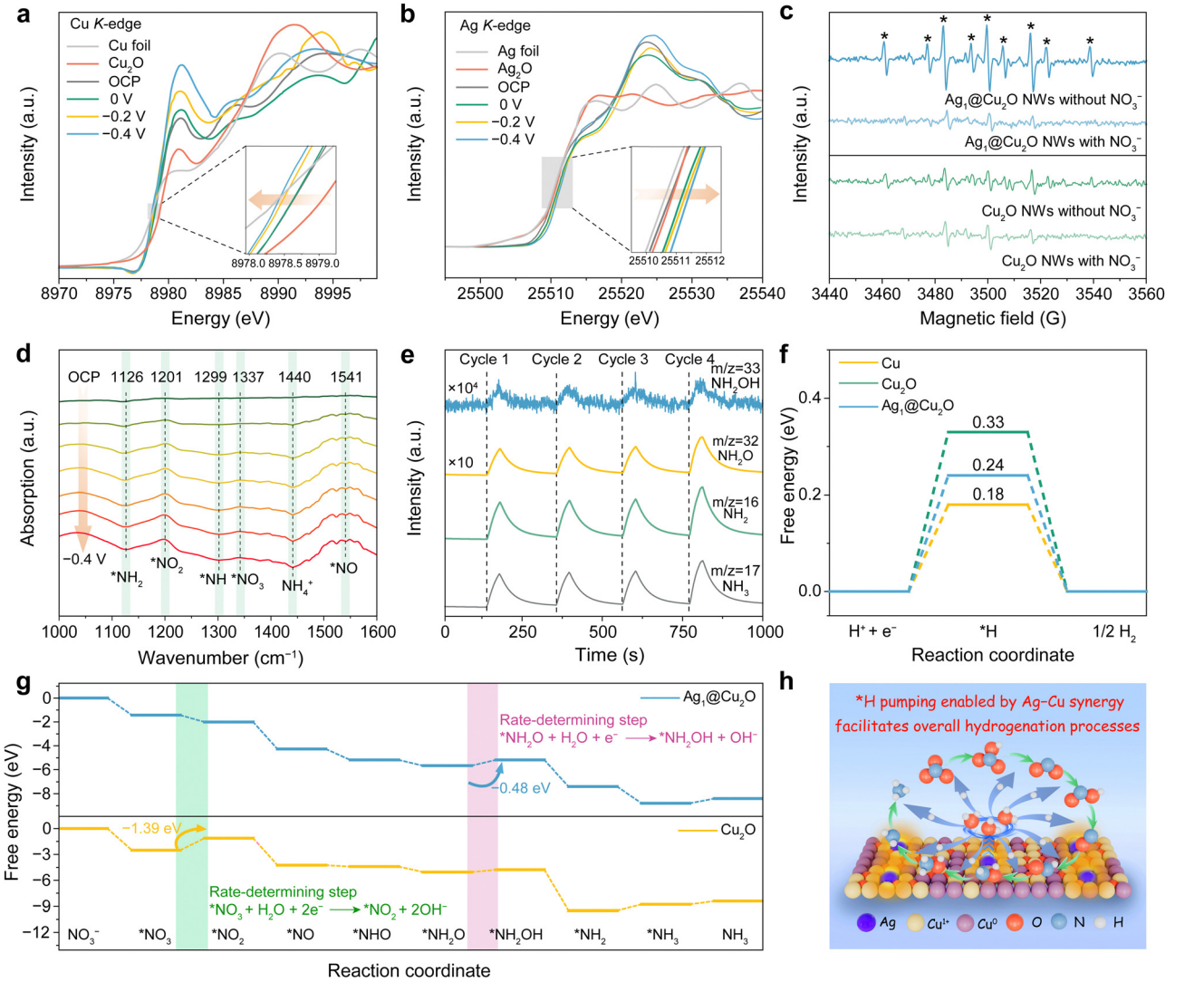

Fig. 4 Mechanistic study of electrocatalytic NO_3^-RR on $Ag_1@Cu_2O$ NWs. (a) *In situ* Cu K-edge XANES spectra. (b) *In situ* Ag K-edge XANES spectra. (c) Quasi-*in situ* EPR spectra at −0.1 V. (d) *In situ* ATR-FTIR. (e) Online DEMS. (f) Gibbs free energy diagrams for *H adsorption on Cu, Cu_2O and $Ag_1@Cu_2O$. (g) Gibbs free energy diagrams of NO_3^-RR on $Ag_1@Cu_2O$ and Cu_2O. (h) Schematic diagram of the Ag–Cu inter-site synergy working in NO_3^-RR.

To gain insights into the NO_3^-RR pathway on $Ag_1@Cu_2O$ NWs, *in situ* attenuated total reflectance Fourier transform infrared (ATR-FTIR) and differential electrochemical mass spectrometry (DEMS) techniques were employed to identify the N-containing intermediates during the NO_3^-RR process from OCP to −0.4 V. The ATR-FTIR analysis shown in Fig. 4(d) identifies distinct absorption peaks for $*NO_3$ at approximately 1337 cm^{-1} and for NH_4^+ around 1440 cm^{-1}, alongside the deoxygenated intermediates ($*NO_2$ at ~1201 cm^{-1} and *NO at ~1541 cm^{-1}) observed in the positive band and hydrogenated intermediates ($*NH_2$ at ~1126 cm^{-1} and *NH at ~1299 cm^{-1}) in the negative band.[3,38] An increase in peak intensities of these deoxygenation/hydrogenation intermediates with decreasing potential was observed. Furthermore, online DEMS corroborated the presence of these intermediates by detecting characteristic *m*/*z* signals, including $*NO_2$ (46), *NO (30), *NHO (31), $*NH_2O$ (32), $*NH_2OH$ (33), $*NH_2$ (16) and NH_3 (17) (Fig. 4(e) and Fig. S34, S35a, ESI†).[3,39] Notably, the intensity of the H_2 signal is two orders of magnitude lower than that of the NH_3 signal at the same potential, indicating a minimal HER side reaction (Fig. S35b, ESI†). Upon cessation of the applied potential, all signals dropped immediately, and the NH_3 signal was virtually invisible when using an NO_3^--free electrolyte, confirming that all detected N-containing intermediates were generated *in situ* during the NO_3^-RR process rather than from external contaminants. The presence of the crucial intermediates of $*NH_2O$ and $*NH_2OH$ supports the NO_3^-RR process on $Ag_1@Cu_2O$ NWs predominantly adhering to the *NHO pathway for NH_3 synthesis (Fig. S36, ESI†).[40]

Further DFT calculations were performed to underpin the proposed Ag single-atom-intensified NO_3^-RR activity of $Ag_1@Cu_2O$ NWs. The charge-density difference analysis upon NO_3^- adsorption revealed significant electron localization at the $Ag_1@Cu_2O$–$*NO_3$ interface compared to the Cu_2O–$*NO_3$

interface, suggesting more favorable charge transfer between $*NO_3$ and $Ag_1@Cu_2O$ (Fig. S37, ESI†).[9,41] Moreover, projected density of states (PDOS) analysis showed a downshift in the d-band center of $Ag_1@Cu_2O$ (−2.07 eV) relative to that of Cu_2O (−1.99 eV) (Fig. S38, ESI†). This shift results in an optimized interaction between $Ag_1@Cu_2O$ and $*NO_3$, facilitating the effective destabilization of $*NO_3$ on $Ag_1@Cu_2O$, and thereby lowering the energy barrier for the initial hydrogenation of $*NO_3$ (Fig. S39, ESI†).[42] Additionally, the Gibbs free energy calculations for *H adsorption indicated that the Cu site in $Ag_1@Cu_2O$ exhibits a stronger affinity for *H compared to Cu_2O, albeit weaker than metallic Cu (Fig. 4(f) and Table S6, ESI†). This finding aligns with experimental observations indicating that the incorporation of Ag single-atoms into Cu_2O significantly facilitates the generation of active *H. It also supports the hypothesis that the *in situ* evolved Cu^0 in $Ag_1@Cu_2O$ serves as the H_2O dissociation site for the generation and stabilization of the active *H for subsequent hydrogenation reactions, rather than primarily promoting *H desorption for HER, as observed in Cu foam during the NO_3^-RR.[43,44] Fig. 4(g) illustrates the Gibbs free energy profiles for NO_3^-RR on Cu sites for Cu_2O and $Ag_1@Cu_2O$ *via* the *NHO pathway (Table S7, ESI†), with detailed adsorption configurations shown in Fig. S40 and S41 (ESI†). The results indicate that the initial $*NO_3 \rightarrow *NO_2$ transformation with an energy barrier of 1.39 eV is considered the rate-determining step (RDS) on Cu_2O. Conversely, the energy barrier of RDS on $Ag_1@Cu_2O$, characterized as $*NH_2O \rightarrow *NH_2OH$, is notably diminished to 0.48 eV. This reduction indicates that the enhanced active *H generation and stabilization capability of $Ag_1@Cu_2O$ not only remarkably lowers the energy barrier for the initial $*NO_3$ deoxygenation process but also optimizes the following overall hydrogenation processes, thus enhancing the NO_3^-RR activity. This matched timely *H supply and smoothed hydrogenation of N-containing intermediates finally gives rise to the high-rate of NO_3^--to-NH_3 conversion achieved on $Ag_1@Cu_2O$ (Fig. 4(h)).

Electrocatalytic FOR performance

Motivated by the high performance of $Ag_1@Cu_2O$ NWs in NO_3^-RR, their potential for catalyzing the formaldehyde (HCHO) oxidation reaction (FOR) was subsequently investigated. This exploration seeks to supplant the thermodynamically unfavorable and value-less anodic OER with FOR to pair with cathodic NO_3^-RR. This pair aims to reduce the overall energy input and simultaneously acquire the valuable formate (HCOOH) product. The electrocatalytic FOR performance of $Ag_1@Cu_2O$ NWs and control samples were assessed in an optimum electrolyte containing 1 M KOH and 0.2 M HCHO (Fig. S42, ESI†). As depicted by the LSVs in Fig. 5(a), $Ag_1@Cu_2O$ NWs display a pronounced FOR current density, reaching 100 mA cm^{-2} at a mere 0.04 V and 300 mA cm^{-2} at 0.31 V, far surpassing the performance of Cu_2O NWs and the negligible activity observed on Cu foam. This exceptional performance of $Ag_1@Cu_2O$ NWs also exceeds those of the majority of previously reported FOR catalysts (Table S8, ESI†). Besides the liquid formate product, significant H_2 production was concurrently

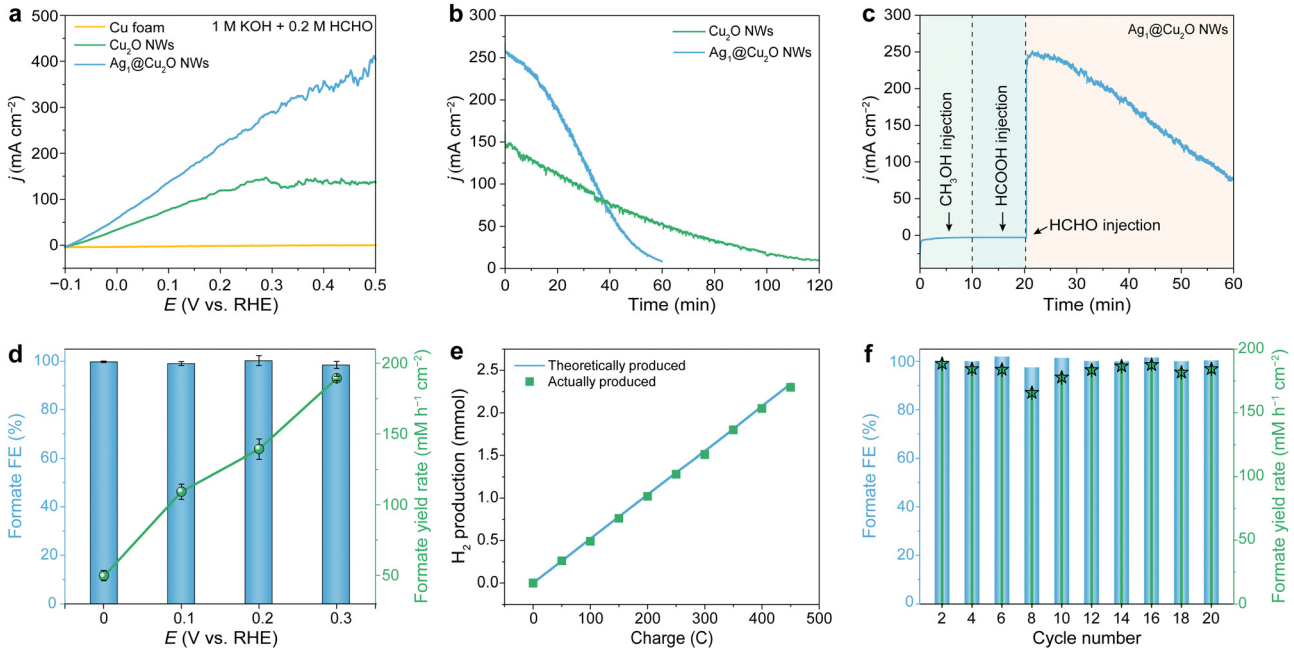

Fig. 5 Electrocatalytic FOR performance. (a) LSVs of $Ag_1@Cu_2O$ NWs, Cu_2O NWs, and Cu foam in 1 M KOH with 0.2 M HCHO. (b) *I*–*t* curves of $Ag_1@Cu_2O$ NWs and Cu_2O NWs at 0.3 V in 1 M KOH with 0.2 M HCHO. (c) *I*–*t* curve of $Ag_1@Cu_2O$ NWs at 0.3 V in 1 M KOH with the sequential addition of 0.2 M CH_3OH, 0.2 M HCOOH, and 0.2 M HCHO. (d) Formate FEs and yield rates on $Ag_1@Cu_2O$ NWs at various potentials. (e) H_2 production amount collected during FOR at 0.3 V. (f) Formate FEs and yield rates on $Ag_1@Cu_2O$ NWs during 20 periods of continuous 1 h stability measurement at 0.3 V in 1 M KOH and 0.2 M HCHO. Error bars represent the standard deviation of at least three independent measurements, with the central value being their average.

observed at the electrode, as evidenced by intense bubbling and confirmed by gas chromatography (GC). The H_2 peak intensity escalated with decreasing potential (Fig. S43, ESI†), highlighting the superiority of electrocatalytic FOR in affording dual high-value fuels of formate and H_2. Further evidence of the superior electrocatalytic FOR activity of $Ag_1@Cu_2O$ NWs was provided by a chronoamperometry test at 0.3 V, which revealed more rapid current attenuation compared to Cu_2O NWs, with the current dropping to nearly 0 within 1 h, indicating the fast and complete oxidative depletion of HCHO (Fig. 5(b)).

To exclude the current contribution from the oxidation of formate product or methanol additive (a stabilizer in commercial 37 wt% HCHO solution) during FOR, their oxidation current responses were examined *via* chronoamperometry at 0.3 V. As shown in Fig. 5(c), the sequential addition of 0.2 M methanol and 0.2 M formate to 1 M KOH electrolyte both led to negligible current changes. Conversely, the injection of 0.2 M HCHO induced an immediate sharp rise in current up to 251.7 mA cm^{-2}, consistent with the LSV current density for FOR (Fig. S44, ESI†). These findings suggest that $Ag_1@Cu_2O$ NWs possess high FOR selectivity and strong tolerance to other electrolyte impurities. This specificity may arise from the relatively low dissociation energy of the C–H bond in HCHO, which facilitates its preferential cleavage over methanol or formate, thereby ensuring superior selectivity and effectively preventing the over-oxidation of formate product to CO_2.[24] In addition, to rule out a non-electrochemical contribution to formate generation during FOR, ^1H NMR analysis was performed for the same 0.2 M HCHO-laden 1 M KOH electrolyte after standing for 2 days without an applied bias. The result reveals negligible formate generation, confirming that the formate product is attributable solely to the electrochemical process and not the intermolecular redox disproportionation of HCHO (Fig. S45, ESI†).[45]

The ability to produce formate and H_2 *via* FOR on $Ag_1@Cu_2O$ NWs was further quantitatively analyzed using ^1H NMR and a drainage method, respectively (Fig. S46, ESI†). As shown in Fig. 5(d), $Ag_1@Cu_2O$ NWs demonstrate excellent formate FEs exceeding 98.5% across a broad range of potentials from 0 to 0.3 V. Remarkably, the formate yield rate reaches 4.75 mmol h^{-1} cm^{-2} at 0.3 V, culminating in an HCHO conversion rate of approximately 95%. Concomitantly, the actual H_2 amounts exhibit a close correspondence with the theoretical values, indicating a near-100% H_2 FE, with a calculated H_2 yield rate of 2.3 mmol h^{-1} cm^{-2} (Fig. 5(e) and Table S9, ESI†). Given that the theoretical stoichiometric yields of formate and H_2 in FOR are in a 2 : 1 molar ratio ($2HCHO + 4OH^- - 2e^- \rightarrow 2HCOO^- + H_2 + 2H_2O$), these results not only substantiate the accuracy of both measured yield rates but also confirm that the formate is exclusively produced *via* FOR. Furthermore, 20 repeated testing cycles with each lasting for 1 h for chronoamperometric FOR at 0.3 V demonstrate both stable formate FE and yield rate throughout, underscoring the excellent catalytic stability of $Ag_1@Cu_2O$ NWs (Fig. 5(f)). This superior sustainability can be attributed to the potent reducing properties of HCHO, which spontaneously reduces the electrooxidized Cu^{2+} back to Cu^{1+}. This regeneration likely helps prevent the deactivation of $Ag_1@Cu_2O$ NWs, thereby maintaining robust FOR activity.[46]

Paired NO_3^-RR/FOR electrolysis for scalable NH_3 production and fixation

To examine the NH_3 production and fixation capabilities in two-electrode paired NO_3^-RR/FOR electrolysis, an MEA electrolyzer was used (Fig. 6(a) and Fig. S47, ESI†), and 1 M KOH + 0.1 M KNO_3 and 1 M KOH + 0.8 M HCHO were employed as the catholyte and anolyte, respectively. As shown in Fig. 6(b), the LSV curve for the coupled NO_3^-RR/FOR electrolysis on $Ag_1@Cu_2O$ NWs reveals an ultralow cell voltage of 0.01 V to reach a current density of 100 mA cm^{-2}, which is 1.69 V and 0.64 V lower than that required for the NO_3^-RR/OER pair with HCHO-free 1 M KOH anolyte and the HER/FOR pair with NO_3^--free 1 M KOH catholyte, respectively, highlighting the energy-saving merit of the NO_3^-RR/FOR couple. More impressively, it requires only 1.6 V to attain a large current density of 600 mA cm^{-2}, representing the best reported cell performance for NH_3 electrosynthesis (Table S10, ESI†). Comprehensive analyses of the cathodic and anodic products from the NO_3^-RR/FOR electrolysis within the potential range of 0.8 to 1.8 V were then conducted (Fig. 6(c) and Fig. S48, ESI†). At the cathode, the maximal NH_3 FE reaches 96% at 1.6 V, corresponding to an NH_3 yield rate of 37.6 mg h^{-1} cm^{-2}. At the anode, the formate FE remains above 97% across all cell voltages, achieving the highest formate yield rate of 206.8 mM h^{-1} cm^{-2} at 1.8 V. Moreover, after a chronoamperometry test at 1.6 V for 5 h, the cumulative formate yield approaches 97.4% (Fig. 6(d)). Throughout the coupled electrolysis, no evident H_2 bubbles were observed at the cathode during NO_3^-RR, while distinct H_2 bubble formation was noted at the anode during FOR (Movie S2, ESI†). This observation indicates that both HCHO and NO_3^- in the electrolytes are essentially transformed, thus laying a solid foundation for subsequent isolation and purification endeavors for upgrading NH_3 into $HCOONH_4$. It should be noted that the paired NO_3^-RR/FOR electrolysis can spontaneously occur without external electricity input due to its inherent primary cell nature ($E^\circ_{cell} = 0.91$ V). Therefore, the performance of this primary cell was compared with that of the MEA-based electrolytic cell. As shown in Fig. S49, ESI,† this primary cell exhibits a limited open circuit voltage (OCV) of 0.52 V and a maximum discharge current density of 80.3 mA cm^{-2}, resulting in a peak power density of only 6.6 mW cm^{-2}. Moreover, it could sustain a discharge current density of 50 mA cm^{-2} for just 1 h, with an NH_3 yield rate of 3.5 mg h^{-1} cm^{-2}, which is significantly lower than that achieved by the MEA-based electrolytic cell. Therefore, this primary cell is unsuitable for implementation in scalable NH_3 production.

To achieve the tandem electrochemical–chemical synthesis of high-value $HCOONH_4$, MEA-based paired NO_3^-RR/FOR electrolysis was performed at 1.6 V, yielding NH_3 and formate products in the cathodic and anodic chambers, respectively. Both the FEs and yield rates for the NH_3 and formate remained stable over prolonged electrolysis of 100 h (Fig. S50, ESI†). Following electrolysis, the anolyte and catholyte were

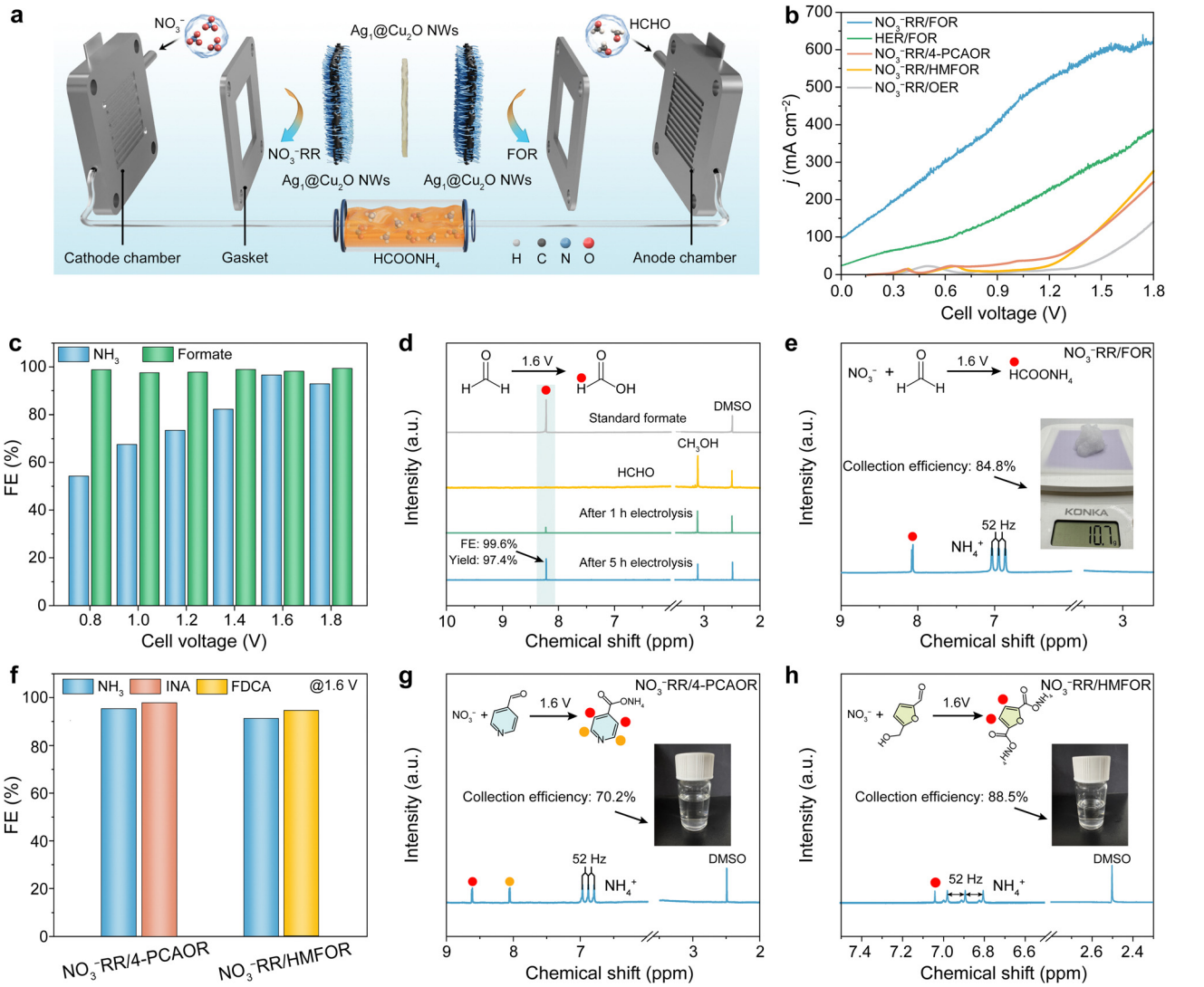

Fig. 6 Paired NO_3^-RR/FOR electrolysis in an MEA electrolyzer for 10 g-scale $HCOONH_4$ synthesis. (a) Schematic illustration of the configuration of the MEA electrolyzer. (b) Performance of MEA-based electrolysis for the NO_3^-RR/OER, NO_3^-RR/FOR, NO_3^-RR/4-PCAOR, and NO_3^-RR/HMFOR pairs. (c) Formate and NH_3 FEs of paired NO_3^-RR/FOR electrolysis within the range 0.8 to 1.8 V. (d) ^{1}H NMR spectra of the anodic formate product from the paired NO_3^-RR/FOR electrolysis. (e) ^{1}H NMR spectrum of the $HCOONH_4$ product; inset is a photograph of the 10.7 g of $HCOONH_4$ solid isolated. (f) FEs of anodic acid and cathodic NH_3 from the paired NO_3^-RR/4-PCAOR and NO_3^-RR/HMFOR electrolysis at 1.6 V. (g) ^{1}H NMR spectrum of the ammonium isonicotinic acid product isolated post-electrolysis at 1.6 V; inset is a photograph of the pure aqueous solution of ammonium isonicotinic acid (0.23 M). (h) ^{1}H NMR spectra of the ammonium furandicarboxylic acid product isolated post-electrolysis at 1.6 V; inset is a photograph of the pure aqueous solution of ammonium furandicarboxylic acid (0.44 M).

thoroughly mixed and subjected to chemical processes of acid neutralization, distillation, and rotary evaporation (see Materials and methods for details). This process results in the successful separation and recovery of pure solid $HCOONH_4$ product and K_2SO_4 byproduct. Remarkably, a total treatment of 0.2 mol NO_3^- and 1.6 mol HCHO, enabled the retrieval of 10.7 g of $HCOONH_4$ solid with a collection efficiency of 84.8% (Fig. 6(e)). The high purity of the $HCOONH_4$ product was confirmed by the ^{1}H NMR spectrum, which indicates complete transformation of NO_3^- and HCHO with no detectable impurity peaks. Additionally, 17.02 g of high-purity solid K_2SO_4 byproduct was simultaneously harvested, as confirmed by XRD analysis (Fig. S51, ESI†). Notably, this synthetic route does not produce any additional pollutants, and all feedstocks are recovered, ensuring complete recycling. Moreover, preliminary cost–benefit analysis estimates the production cost of $HCOONH_4$ could potentially be as low as \$237.4 ton^{-1}, approximately 30% of its commercial commodity price (Note S1, ESI†). This highlights the significant potential of this route for efficient NO_3^-/HCHO sewage purification and economically viable large-scale NH_3 production and upgrading into high-value $HCOONH_4$.

To evaluate the applicability of this tandem electrochemical–chemical synthetic strategy for upgrading NH_3 into other ammonium acid salts, we further investigated the coupling of NO_3^-RR with oxidation of higher aldehydes. Specifically, two other representative five- and six-membered heterocyclic

aldehydic compounds, 5-hydroxymethylfurfural (HMF) and 4-pyridinecarboxaldehyde (4-PCA), were selected as anodic substrates for coupling electrolysis. As shown in Fig. 6(b), LSV curves for the NO_3^-RR/HMFOR and NO_3^-RR/4-PCAOR electrolysis exhibit comparable current densities, both superior to that for NO_3^-RR/OER, demonstrating the consistent high performance of $Ag_1@Cu_2O$ NWs across these pairs. At the same voltage of 1.6 V for 2 h and 5 h, the measured cathodic NH_3 FEs are 95.2% for NO_3^-RR/4-PCAOR and 91% for NO_3^-RR/HMFOR, respectively, indicating sustained catalytic activity despite the variation in anodic aldehydes (Fig. 6(f)). The corresponding anodic products, isonicotinic acid (INA) from 4-PCAOR and furan-2,5-dicarboxylic acid (FDCA) from HMFOR, were quantitatively analyzed by ^{1}H NMR spectroscopy (Fig. S52 and S53, ESI†). The calculated FEs are 95.3% for INA and 98.9% for FDCA, with corresponding yields of 98.7% and 97.4% (Fig. S54, ESI†). The absence of impurity peaks in the ^{1}H NMR spectra underscores the remarkable activity and selectivity of $Ag_1@Cu_2O$ NWs for the electrooxidation of these heterocyclic aldehydes. Finally, the cathodic NH_3 product was fixed using pure INA or FDCA powders isolated from the corresponding anolyte, leading to aqueous solutions of ammonium isonicotinic acid (0.23 M) and ammonium furandicarboxylic acid (0.44 M), with high collection efficiencies of 70.2% and 88.5%, respectively, and their high purity was verified by ^{1}H NMR spectroscopy (Fig. 6(g) and (h)). These expansions successfully showcase the adaptability of this route for scalable NH_3 fixation and upgrading into high-value chemicals from the valorization of nitrate and various industrial pollutants, demonstrating its broad applicability and both potential industrial and environmental benefits.

Conclusions

A high-performance bifunctional single-atom electrocatalyst, $Ag_1@Cu_2O$ NWs, has been successfully developed for both nitrate reduction and formaldehyde oxidation. This catalyst exhibits high-rate nitrate-to-ammonia conversion across a wide range of nitrate concentrations, achieving a two-ampere-level current density of 2.3 A cm^{-2} along with a notable NH_3 yield rate of 184.4 mg h^{-1} cm^{-2} at 0.5 M nitrate concentration. Using a combination of *in situ* techniques and DFT calculations, it has been elucidated that the Ag–Cu inter-site electronic synergy plays a pivotal role in accelerating active *H supply, which in turn facilitates the hydrogenation of N-containing intermediates occurring on the *in situ* evolved Cu/Cu_2O heterostructure *via* the *NHO reaction pathway. This ultimately leads to significantly enhanced hydrogenation kinetics of NO_3^-RR on $Ag_1@Cu_2O$ NWs, and hence accelerated ammonia production. For formaldehyde oxidation, $Ag_1@Cu_2O$ NWs achieve a large current density of 300 mA cm^{-2} at 0.31 V *vs.* RHE, concurrently producing formate and H_2 with near-100% FE. Motivated by this superb bifunctionality of $Ag_1@Cu_2O$ NWs, a tandem electrochemical–chemical route for the scalable fixation of the produced ammonia into 10.7 g of $HCOONH_4$ solid has been demonstrated by coupling NO_3^-RR and FOR in MEA-based electrolysis. The adaptability of this strategy has been validated by its successful extension to two more nitrate/aldehyde pairs. This study not only provides a versatile high-current-density electrocatalyst but also potentially inspires broader future efforts towards more diverse and scalable green ammonia fixation and valorization from nitrate electroreduction.

Author contributions

L. Z. designed this study and, along with Y. C., was responsible for most of the investigations, methodology development, data collection and analysis, visualization and writing of the original manuscript. Y. L. and D. C. assisted with data collection and analysis. H.-T. W., C.-F. L. and T.-S. C. performed the *ex situ* XAFS measurements. H. I., N. H. and Y.-C. S. helped with the *in situ* XAFS measurements. C. S. performed the electron tomography for 3D reconstruction. D. X. conducted the AC-STEM characterizations. S. F. and Y. W. performed the EELS mapping. Y. X. and Y. Y. executed the DFT calculations. X. W. and J. L. contributed valuable discussions on the data analysis. L. H. supervised the project, directed the study, and revised the manuscript. All authors approve the final manuscript.

Data availability

All data supporting this article have been included in the paper and the ESI.† Additional data related to this paper can be provided upon request from the corresponding author.

Conflicts of interest

There are no conflicts to declare.

Acknowledgements

This work was supported by the National Key Research and Development Program of China (2022YFA1505700), National Natural Science Foundation of China (22475214, 22205232, 22222801 and 21601187), Talent Plan of Shanghai Branch, Chinese Academy of Sciences (CASSHB-QNPD-2023-020), Natural Science Foundation of Fujian Province (2023J06044 and 2023J01213), and the Self-deployment Project of Haixi Institutes, Chinese Academy of Sciences (CXZX-2022-JQ06 and CXZX-2022-GH03). The XAFS study on beamline TLS 01C1 at National Synchrotron Radiation Research Center (NSRRC) and beamline BL12XU at SPring-8 (Japan) is highly acknowledged. The authors also greatly appreciate support by Transmission Electron Microscope Platform and High-performance Computing Platform of Fujian Science & Technology Innovation Laboratory for Optoelectronic Information of China.

Notes and references

1 C. Q. Yu, X. Huang, H. Chen, H. C. J. Godfray, J. S. Wright, J. W. Hall, P. Gong, S. Q. Ni, S. C. Qiao, G. R. Huang, Y. C. Xiao, J. Zhang, Z. Feng, X. T. Ju, P. Ciais, N. C. Stenseth, D. O. Hessen, Z. L. Sun, L. Yu, W. J. Cai, H. H. Fu, X. M. Huang, C. Zhang, H. B. Liu and J. Taylor, *Nature*, 2019, **567**, 516–520.

2 K. Wang, R. Mao, R. Liu, J. Zhang, H. Zhao, W. Ran and X. Zhao, *Nat. Water*, 2023, **1**, 1068–1078.

3 S. Han, H. Li, T. Li, F. Chen, R. Yang, Y. Yu and B. Zhang, *Nat. Catal.*, 2023, **6**, 402–414.

4 J. Y. Fang, Q. Z. Zheng, Y. Y. Lou, K. M. Zhao, S. N. Hu, G. Li, O. Akdim, X. Y. Huang and S. G. Sun, *Nat. Commun.*, 2022, **13**, 7899.

5 Z. Chang, G. Meng, Y. Chen, C. Chen, S. Han, P. Wu, L. Zhu, H. Tian, F. Kong, M. Wang, X. Cui and J. Shi, *Adv. Mater.*, 2023, **35**, e2304508.

6 Y.-M. Cai, Y.-H. Li, Y. Xiao, Q. Meyer, Q. Sun, W.-J. Lai, S.-W. Zhao, J. Li, L.-J. Zhang, H. Wang, Z. Lin, J. Luo and L.-L. Han, *Rare Met.*, 2024, **43**, 5792–5801.

7 Z. Song, Y. Liu, Y. Zhong, Q. Guo, J. Zeng and Z. Geng, *Adv. Mater.*, 2022, **34**, e2204306.

8 W. He, J. Zhang, S. Dieckhofer, S. Varhade, A. C. Brix, A. Lielpetere, S. Seisel, J. R. C. Junqueira and W. Schuhmann, *Nat. Commun.*, 2022, **13**, 1129.

9 J. Dai, Y. Tong, L. Zhao, Z. Hu, C. T. Chen, C. Y. Kuo, G. Zhan, J. Wang, X. Zou, Q. Zheng, W. Hou, R. Wang, K. Wang, R. Zhao, X. K. Gu, Y. Yao and L. Zhang, *Nat. Commun.*, 2024, **15**, 88.

10 J. Sun, H. Yang, W. Gao, T. Cao and G. Zhao, *Angew. Chem., Int. Ed.*, 2022, **61**, e202211373.

11 M. Xie, S. Tang, Z. Li, M. Wang, Z. Jin, P. Li, X. Zhan, H. Zhou and G. Yu, *J. Am. Chem. Soc.*, 2023, **145**, 13957–13967.

12 F. Xie, X. Cui, X. Zhi, D. Yao, B. Johannessen, T. Lin, J. Tang, T. B. F. Woodfield, L. Gu and S.-Z. Qiao, *Nat. Synth.*, 2023, **2**, 129–139.

13 F. Y. Chen, Z. Y. Wu, S. Gupta, D. J. Rivera, S. V. Lambeets, S. Pecaut, J. Y. T. Kim, P. Zhu, Y. Z. Finfrock, D. M. Meira, G. King, G. Gao, W. Xu, D. A. Cullen, H. Zhou, Y. Han, D. E. Perea, C. L. Muhich and H. Wang, *Nat. Nanotechnol.*, 2022, **17**, 759–767.

14 J. Li, H. Li, K. Fan, J. Y. Lee, W. Xie and M. Shao, *Chem. Catal.*, 2023, **3**, 100638.

15 W. Guo, S. Zhang, J. Zhang, H. Wu, Y. Ma, Y. Song, L. Cheng, L. Chang, G. Li, Y. Liu, G. Wei, L. Gan, M. Zhu, S. Xi, X. Wang, B. I. Yakobson, B. Z. Tang and R. Ye, *Nat. Commun.*, 2023, **14**, 7383.

16 R. Gao, T. Y. Dai, Z. Meng, X. F. Sun, D. X. Liu, M. M. Shi, H. R. Li, X. Kang, B. Bi, Y. T. Zhang, T. W. Xu, J. M. Yan and Q. Jiang, *Adv. Mater.*, 2023, **35**, e2303455.

17 W. Zhu, F. Yao, Q. Wu, Q. Jiang, J. Wang, Z. Wang and H. Liang, *Energy Environ. Sci.*, 2023, **16**, 2483–2493.

18 S. Verma, S. Lu and P. J. A. Kenis, *Nat. Energy*, 2019, **4**, 466–474.

19 Q. Qian, X. He, Z. Li, Y. Chen, Y. Feng, M. Cheng, H. Zhang, W. Wang, C. Xiao, G. Zhang and Y. Xie, *Adv. Mater.*, 2023, **35**, e2300935.

20 G. Han, G. Li and Y. Sun, *Nat. Catal.*, 2023, **6**, 224–233.

21 Z. J. Schiffer, S. Biswas and K. Manthiram, *ACS Energy Lett.*, 2022, **7**, 3260–3267.

22 Z. Pan, Z. Zhang, W. Li, X. Huo, Y. Liu, O. C. Esan, Q. Wu and L. An, *ACS Energy Lett.*, 2023, **8**, 3742–3749.

23 R. Siya and E. E. Richard, *Synthesis*, 1988, 91–95.

24 G. Li, G. Han, L. Wang, X. Cui, N. K. Moehring, P. R. Kidambi, D. E. Jiang and Y. Sun, *Nat. Commun.*, 2023, **14**, 525.

25 Y. Liu, Z. Zhuang, Y. Liu, N. Liu, Y. Li, Y. Cheng, J. Yu, R. Yu, D. Wang and H. Li, *Angew. Chem., Int. Ed.*, 2024, **63**, e202411396.

26 L. J. Zhang, N. Jin, Y. B. Yang, X. Y. Miao, H. Wang, J. Luo and L. L. Han, *Nano-Micro Lett.*, 2023, **15**, 228.

27 H. Yadegari, A. Ozden, T. Alkayyali, V. Soni, A. Thevenon, A. Rosas-Hernandez, T. Agapie, J. C. Peters, E. H. Sargent and D. Sinton, *ACS Energy Lett.*, 2021, **6**, 3538–3544.

28 C. Du, J. P. Mills, A. G. Yohannes, W. Wei, L. Wang, S. Lu, J. X. Lian, M. Wang, T. Guo, X. Wang, H. Zhou, C. J. Sun, J. Z. Wen, B. Kendall, M. Couillard, H. Guo, Z. Tan, S. Siahrostami and Y. A. Wu, *Nat. Commun.*, 2023, **14**, 6142.

29 A. A. Guda, S. A. Guda, A. Martini, A. N. Kravtsova, A. Algasov, A. Bugaev, S. P. Kubrin, L. V. Guda, P. Šot, J. A. van Bokhoven, C. Copéret and A. V. Soldatov, *npj Comput. Mater.*, 2021, **7**, 203.

30 L. Cao, Q. Luo, W. Liu, Y. Lin, X. Liu, Y. Cao, W. Zhang, Y. Wu, J. Yang, T. Yao and S. Wei, *Nat. Catal.*, 2018, **2**, 134–141.

31 W. Yu, J. Yu, M. Huang, Y. Wang, Y. Wang, J. Li, H. Liu and W. Zhou, *Energy Environ. Sci.*, 2023, **16**, 2991–3001.

32 H. Xu, Y. Y. Ma, J. Chen, W. X. Zhang and J. P. Yang, *Chem. Soc. Rev.*, 2022, **51**, 2710–2758.

33 S. Y. Xiang, Y. H. Liu, G. M. Zhang, R. Ruan, Y. P. Wang, X. D. Wu, H. L. Zheng, Q. Zhang and L. P. Cao, *World J. Microbiol. Biotechnol.*, 2020, **36**, 144.

34 Q. Hu, K. Yang, O. Peng, M. Li, L. Ma, S. Huang, Y. Du, Z. X. Xu, Q. Wang, Z. Chen, M. Yang and K. P. Loh, *J. Am. Chem. Soc.*, 2024, **146**, 668–676.

35 Y. Wang, W. Zhou, R. Jia, Y. Yu and B. Zhang, *Angew. Chem., Int. Ed.*, 2020, **59**, 5350–5354.

36 Y. Bu, C. Wang, W. Zhang, X. Yang, J. Ding and G. Gao, *Angew. Chem., Int. Ed.*, 2023, **62**, e202217337.

37 G. Zhang, X. Li, K. Chen, Y. Guo, D. Ma and K. Chu, *Angew. Chem., Int. Ed.*, 2023, **62**, e202300054.

38 H. Liu, X. Lang, C. Zhu, J. Timoshenko, M. Ruscher, L. Bai, N. Guijarro, H. Yin, Y. Peng, J. Li, Z. Liu, W. Wang, B. R. Cuenya and J. Luo, *Angew. Chem., Int. Ed.*, 2022, **61**, e202202556.

39 L. Wu, J. Feng, L. Zhang, S. Jia, X. Song, Q. Zhu, X. Kang, X. Xing, X. Sun and B. Han, *Angew. Chem., Int. Ed.*, 2023, **62**, e202307952.

40 J. Wang, C. Cai, Y. A. Wang, X. M. Yang, D. J. Wu, Y. M. Zhu, M. H. Li, M. Gu and M. H. Shao, *ACS Catal.*, 2021, **11**, 15135–15140.

41 L. J. Zhang, T. T. Gu, K. L. Lu, L. J. Zhou, D. S. Li and R. H. Wang, *Adv. Funct. Mater.*, 2021, **31**, 2103187.

42 K. Chen, Z. Ma, X. Li, J. Kang, D. Ma and K. Chu, *Adv. Funct. Mater.*, 2023, **33**, 2209890.
43 P. Li, J. Bi, J. Liu, Q. Zhu, C. Chen, X. Sun, J. Zhang and B. Han, *Nat. Commun.*, 2022, **13**, 1965.
44 L. Zhang, H. Hu, C. Sun, D. Xiao, H.-T. Wang, Y. Xiao, S. Zhao, K. H. Chen, W.-X. Lin, Y.-C. Shao, X. Wang, C.-W. Pao and L. Han, *Nat. Commun.*, 2024, **15**, 7179.
45 Y. Pan, Y. Li, C.-L. Dong, Y.-C. Huang, J. Wu, J. Shi, Y. Lu, M. Yang, S. Wang and Y. Zou, *Chem*, 2023, **9**, 963–977.
46 R. Cai, M. Sun, F. Yang, M. Ju, Y. Chen, M. D. Gu, B. Huang and S. Yang, *Chem*, 2024, **10**, 211–233.

